Editors' Suggestion

Magnetic phase diagram of a two-orbital model for bilayer nickelates with varying doping

Ling-Fang Lin,[1,*] Yang Zhang,[1,†] Nitin Kaushal,[2] Gonzalo Alvarez,[3] Thomas A. Maier,[3] Adriana Moreo,[1,4] and Elbio Dagotto[1,4]

[1]*Department of Physics and Astronomy, University of Tennessee, Knoxville, Tennessee 37996, USA*
[2]*Department of Physics and Astronomy and Quantum Matter Institute, University of British Columbia, Vancouver, British Columbia BC V6T 1Z4, Canada*
[3]*Computational Sciences and Engineering Division, Oak Ridge National Laboratory, Oak Ridge, Tennessee 37831, USA*
[4]*Materials Science and Technology Division, Oak Ridge National Laboratory, Oak Ridge, Tennessee 37831, USA*

(Received 10 August 2024; revised 9 October 2024; accepted 31 October 2024; published 18 November 2024)

Motivated by the recently discovered high-T_c bilayer nickelate superconductor $La_3Ni_2O_7$, we comprehensively research a bilayer $2 \times 2 \times 2$ cluster for different electronic densities n by using the Lanczos method. We also employ the random-phase approximation to quantify the first magnetic instability with increasing Hubbard coupling strength, also varying n. Based on the spin structure factor $S(q)$, we have obtained a rich magnetic phase diagram in the plane defined by n and U/W, at fixed Hund coupling, where U is the Hubbard strength and W the bandwidth. We have observed numerous states, such as A-AFM, Stripes, G-AFM, and C-AFM. At half-filling, $n = 2$ (two electrons per Ni site, corresponding to $N = 16$ electrons), the canonical superexchange interaction leads to a robust G-AFM state (π, π, π) with antiferromagnetic couplings both in-plane and between layers. By increasing or decreasing electronic densities, ferromagnetic tendencies emerge from the "half-empty" and "half-full" mechanisms, leading to many other interesting magnetic tendencies. In addition, the spin-spin correlations become weaker both in the hole or electron doping regions compared with half-filling. At $n = 1.5$ (or $N = 12$), density corresponding to $La_3Ni_2O_7$, we obtained the "Stripe 2" ground state (antiferromagnetic coupling in one in-plane direction, ferromagnetic coupling in the other, and antiferromagnetic coupling along the z axis) in the $2 \times 2 \times 2$ cluster. In addition, we obtained a much stronger AFM coupling along the z axis than the magnetic coupling in the xy plane. The random-phase approximation calculations with varying n give very similar results as Lanczos, even though both techniques are based on quite different procedures. Additionally, a state with $q/\pi = (0.6, 0.6, 1)$ close to the E-phase wavevector is found in our RPA calculations by slightly reducing the filling to $n = 1.25$, possibly responsible for the E-phase SDW recently observed in experiments. Our predictions can be tested by chemically doping $La_3Ni_2O_7$.

DOI: 10.1103/PhysRevB.110.195135

I. INTRODUCTION

Since the discovery of superconductivity in Sr-doped infinite-layer $NdNiO_2$ films [1], nickelates became the newest member of the family of high-T_c superconductors [2–7], following the copper- and iron-based families [8–11]. Very recently, a record $T_c \sim 80$ K superconductivity was reported in bilayer $La_3Ni_2O_7$ under pressure [12], opening a new remarkable avenue for the study of unconventional superconductivity [13–39].

$La_3Ni_2O_7$ has a bilayer NiO_6 octahedron stacking layered structure [40], belonging to the Ruddlesden-Popper perovskite family, different from the NiO_4 layered nickelates [1,2]. At ambient pressure, $La_3Ni_2O_7$ has an orthorhombic Amam (No. 63) atomic structure with an $(a^-a^-c^0)$ out-of-phase octahedron tilting distortion around the [110] axis originating from the high-symmetry I4/mmm phase [40]. By introducing hydrostatic pressure, a first-order phase transition from Amam to Fmmm (No. 69) phases was obtained, fully suppressing the NiO_6 octahedron tilting rotations around 10 GPa [see Fig. 1(a)]. In this symmetric phase, superconductivity was found in a broad pressure range from 14 to 43.5 GPa [12]. In addition, the tetragonal I4/mmm phase has also been proposed to represent the high-pressure structure in both theory [41] and experiments [42]. However, those two phases provide basically the same physics [43] because the distortion from I4/mmm to Fmmm is very small [44].

The early report of superconductivity under pressure was based on a sharp drop and flat stage in resistance vs temperature, found by using KBr as the pressure-transmitting medium [12]. Moreover, a diamagnetic response in the susceptibility was reported, and those results were interpreted as an indication of both zero resistance and Meissner effect [12], suggesting a superconducting state. Zero resistance was later confirmed by several studies [14,15,17]. Very recently, the Meissner effect of the superconducting state was observed in the *ac* magnetic susceptibility, with the superconducting volume fraction up to 48% [45], suggesting bulk superconductivity, as opposed to initial suggestions of filamentary superconductivity [46].

First-principles density functional theory (DFT) calculations suggest that $La_3Ni_2O_7$ has a large charge-transfer gap

*Contact author: lflin@utk.edu
†Contact author: yzhang@utk.edu

 ©2024 American Physical Society

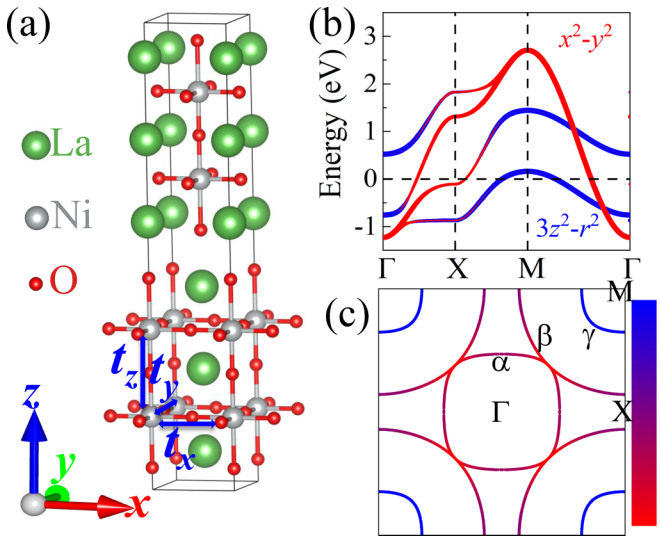

FIG. 1. (a) Crystal structure of $La_3Ni_2O_7$ in the Fmmm phase. The three directions of nearest-neighbor hopping matrices are indicated by t_x, t_y, and t_z. Calculated (b) band structure and (c) Fermi surface with average electronic filling $n = 1.5$ per site for the two-orbital tight-binding model with the nearest-neighbor hopping along the x, y, and z axis in the high-pressure phase.

between Ni's $3d$ and O's $2p$ orbitals and can be described as a Ni two-orbital bilayer model [47,48]. Induced by canonical "dimer" physics [48], the Ni $d_{3z^2-r^2}$ orbital forms a bonding-antibonding molecular-orbital state, while the $d_{x^2-y^2}$ orbital remains decoupled between layers. Because of the in-plane hybridization between e_g orbitals, the electronic occupation of both orbitals are nonintegers [47,49]. In addition, the Fermi surface of $La_3Ni_2O_7$ under pressure consists of two electron sheets (α and β), combinations of mixed e_g orbitals, and a hole pocket γ, made of the $d_{3z^2-r^2}$ orbital [47,48]. This γ pocket was not found in recent angle-resolved photoemission spectroscopy experiments for the nonsuperconducting Amam phase of $La_3Ni_2O_7$ [16]. The random-phase approximation (RPA) many-body calculations suggest that this γ hole pocket, and its associated Fermi surface nesting, plays the key role in mediating superconductivity in $La_3Ni_2O_7$ [50]. In addition, recent DFT calculations also found that the electron-phonon coupling alone is not sufficient to obtain such high T_c in $La_3Ni_2O_7$ under pressure [51–53], but superconductivity could be enhanced by combining the electron-phonon coupling and electronic correlations [53].

Based on the two-orbital model described above, a $s_\pm$-wave pairing superconducting channel induced by spin fluctuations was reported by several theoretical studies, caused by the partial nesting of the Fermi surface in the high-pressure phase of $La_3Ni_2O_7$ [43,50,54–61]. Although the $s_\pm$-wave pairing superconducting channel was considered to be driven by strong interlayer coupling, the $d_{x^2-y^2}$ orbital also has robust contributions to the superconducting gap, comparable to those of the $d_{3z^2-r^2}$ orbital [50,62]. Alternative studies suggest a dominant $d_{x^2-y^2}$-wave superconducting pairing channel arising from the superconducting pairing state in the β sheet [63–65], driven mostly by the intralayer coupling, where this β sheet is similar to that in the optimally doped cuprate superconductor. In addition, by introducing longer-range hoppings, the d_{xy} symmetry pairing channel could also compete with the $s_\pm$-wave symmetry [66,67], also driven by the intralayer coupling. In fact, the interplay between the intralayer and the interlayer Cooper pairing was originally discussed by t–J models in coupled plane or ladder geometries, finding that a strong interlayer coupling leads to s-wave pairing, while strong intralayer coupling would result in d-wave pairing [68].

In addition, $La_3Ni_2O_7$ displays rich and complex density wave behaviors of spin and charge, depending on the pressure and temperature [69–73]. Early experiments involving resistivity measurements reported a kink-like transition behavior around 153 K at ambient pressure, suggesting the existence of a spin-density wave (SDW) [73]. A recent muon-spin relaxation (μSR) experiment revealed the presence of SDW in $La_3Ni_2O_{7-\delta}$ without pressure [72,74]. Furthermore, a nuclear magnetic resonance (NMR) experiment also supports the existence of SDW in $La_3Ni_2O_7$ [75]. Neutron [71] and resonant inelastic x-ray scattering [70] experiments arrive at similar conclusions. However, because of the difficulty with high-pressure experiments, the full evolution of the magnetic properties of $La_3Ni_2O_7$ under pressure is still unclear.

In this paper, using a Lanczos method, we systematically studied a bilayer $2 \times 2 \times 2$ cluster for several electronic densities n [76]. We obtained a very rich magnetic phase diagram varying n, involving the A-AFM, Stripe 2, G-AFM, and C-AFM phases. At half-filling with number of electrons $N = 16$ (or density $n = 2$), because of the canonical superexchange antiferromagnetic (AFM) interaction, the system displays a robust G-AFM state with both AFM couplings in-plane and between planes, in the bilayer geometry. By hole or electron doping away from half-filling, ferromagnetic (FM) tendencies start developing from the "half-empty" and "half-full" mechanisms [77]. Thus, FM competes with AFM tendencies, leading to a rich magnetic phase diagram. Furthermore, the spin-spin correlations become weaker with increasing hole or electron doping away from half-filling. At $N = 12$ ($n = 1.5$), corresponding to the electronic density of Ni in $La_3Ni_2O_7$, we obtained a Stripe 2 ground state (AFM in one in-plane direction and FM in the other, while AFM along the z axis) in our $2 \times 2 \times 2$ cluster calculations, in agreement with multiple previous studies using other approximations. This agreement suggests that our predictions for other densities (reachable by doping $La_3Ni_2O_7$) are robust. In addition, we also obtained a much stronger AFM coupling along the z axis than the magnetic coupling in the xy plane. Complementing our Lanczos study, here we also employ the RPA varying the density n, reporting the leading magnetic instability with increasing Hubbard strength at several fixed densities. Overall, there is very good qualitative agreement between Lanczos and RPA, two very different approximations, again providing a robust foundation to our conclusions.

II. METHODS

In this paper, we employed the standard multiorbital Hubbard model on a cube system ($2 \times 2 \times 2$), which refers to a bilayer lattice of Ni, where each lattice point refers to a Ni position in Fig. 1(a). Specifically, the Hamiltonian includes a kinetic energy component and Coulomb interaction energy

terms $H = H_k + H_{\rm int}$. The tight-binding (TB) kinetic portion is described as

$$H_k = \sum_{<i,j>\sigma\gamma\gamma'} t_{\gamma\gamma'}(c^\dagger_{i\sigma\gamma}c_{j\sigma\gamma'} + H.c.) + \sum_{i\gamma\sigma}\Delta_\gamma n_{i\gamma\sigma}, \quad (1)$$

where the first term represents the hopping of an electron from orbital γ at site i to orbital γ' at site j. γ and γ' represent the two different orbitals. The second term includes the crystal-fields splitting terms.

The electronic interaction portion of the Hamiltonian is (using standard notation)

$$H_{\rm int} = U\sum_{i\gamma} n_{i\uparrow\gamma}n_{i\downarrow\gamma} + \left(U' - \frac{J_{\rm H}}{2}\right)\sum_{\substack{i\\ \gamma<\gamma'}} n_{i\gamma}n_{i\gamma'} - 2J_{\rm H}\sum_{\substack{i\\ \gamma<\gamma'}} \mathbf{S}_{i\gamma}\cdot\mathbf{S}_{i\gamma'} + J_{\rm H}\sum_{\substack{i\\ \gamma<\gamma'}}(P^\dagger_{i\gamma}P_{i\gamma'} + {\rm H.c.}). \quad (2)$$

The first term is the intraorbital Hubbard repulsion. The second term is the electronic repulsion between electrons at different orbitals, where the standard relation $U' = U - 2J_{\rm H}$ is assumed because of rotational invariance. The third term represents the Hund's coupling between electrons occupying the Ni's $3d$ orbitals. The fourth term is the pair hopping between different orbitals at the same site i, where $P_{i\gamma} = c_{i\downarrow\gamma}c_{i\uparrow\gamma}$.

To study the multiorbital Hubbard model, including quantum fluctuations beyond mean-field approximations, the many-body technique that we employed was the Lanczos method, supplemented by the density matrix renormalization group (DMRG) method [78,79]. In practice, we used the `SCS_Lanczos` [80] and DMRG++ software packages [81]. For simplicity, for even electron numbers, the targeting up ($N_{\rm up}$) and down ($N_{\rm dn}$) electrons are equal, corresponding to $S_z = 0$ sector. While for odd electron numbers, the targeting $N_{\rm up} = N_{\rm dn} + 1$, corresponding to $S_z = 1/2$ sector. Both open-boundary conditions (OBC) and periodic-boundary conditions (PBC) were considered along the xy directions, while along the z axis it was always OBC as in bilayers. Because of the special structure of our cluster, the only difference in-plane between PBC and OBC is that we doubled the values of the t_x and t_y hoppings for the PBC case. One thousand Lanczos steps and convergence criterium below 10^{-10} were set during our Lanczos calculations. At several points in parameter space, DMRG calculations were also used to confirm our Lanczos results. We found that the results from Lanczos and DMRG agree very well. During the DMRG calculation, at least 1200 states were kept and up to 21 sweeps were performed.

In the tight-binding term, we used the basis $\{d_{3z^2-r^2}, d_{x^2-y^2}\}$, here referred to as $\gamma = \{0, 1\}$, respectively. For simplicity, we only considered the nearest-neighbor-hopping matr ices along the three directions, which are obtained from our previous first-principles study for $La_3Ni_2O_7$ under pressure by using the crystal structure in Fig. 1(a) [48]. The three nearest-neighbor hopping matrices are shown below:

$$t^x_{\gamma\gamma'} = \begin{bmatrix} -0.115 & 0.240 \\ 0.240 & -0.492 \end{bmatrix}, \quad (3)$$

$$t^y_{\gamma\gamma'} = \begin{bmatrix} -0.115 & -0.240 \\ -0.240 & -0.492 \end{bmatrix}, \quad (4)$$

$$t^z_{\gamma\gamma'} = \begin{bmatrix} -0.644 & 0.000 \\ 0.00 & 0.000 \end{bmatrix}. \quad (5)$$

All the hopping matrix elements are given in eV units. Δ_γ is the crystal-field splitting of orbital γ. Specifically, $\Delta_0 = 0$, $\Delta_1 = 0.398$ eV. The total kinetic energy bandwidth W is 3.936 eV.

III. RESULTS

A. TB results

Before discussing our Lanczos results, the calculated TB electronic structures corresponding to $La_3Ni_2O_7$ under pressure are briefly reviewed here. The Fermi energy is obtained by integrating the density of states for all ω until a number of 1.5 electrons per Ni site is reached. Based on the obtained Fermi energy, a 4001×4001 k mesh was used to calculate the Fermi surface. The odd character of 4001 ensures that the Γ point (0,0) is included in the grid used.

As shown in Fig. 1(b), the $d_{3z^2-r^2}$ orbital displays the expected bonding-antibonding splitting, where the bonding state band goes slightly above the Fermi level, resulting in a γ hole pocket around the M point [see Fig. 1(c)]. In addition, the Fermi surface also contains two electron sheets (α and β) formed from a mixture of $d_{3z^2-r^2}$ and $d_{x^2-y^2}$ orbitals caused by the in-plane hybridization of e_g orbitals. These results are in agreement with previous theoretical studies [47,48,56,59].

The electronic structure of the Amam phase without pressure is quite similar to that of the high-pressure phase, but note that the small hole pocket of bonding state $d_{3z^2-r^2}$ is absent [48] at 0 GPa, as discussed in previous theoretical papers [12,48]. This pocket was also not observed in the angle-resolved photoemission spectroscopy experiment as well [16]. In the Amam phase, the octahedron is strongly distorted and tilted, leading to two different Ni-Ni bonds along the in-plane x and y directions. Furthermore, in the Amam phase, the $d_{yz/xz}$ orbitals are also hybridized with the e_g orbitals, leading to an interorbital hopping between $d_{yz/xz}$ and e_g orbitals that cannot be ignored [48]. This hopping could enhance the ferromagnetic (FM) tendency owing to the "half-full" mechanism [77]. In this case, a two-orbital model maybe not be enough for the Amam phase to study the magnetism properties. Considering these points, the phase diagram of the low-pressure Amam phase may be different from our present results. However, this is a formidable task for Lanczos calculations because it requires increasing sizes and adding orbitals, which is beyond our present capabilities. Note that, in the present paper, our scope focuses on the high-pressure phase that harbors superconductivity, without octahedral tilting, by using a $2 \times 2 \times 2$ cluster Lanczos calculations.

B. Phase diagrams

To obtain the magnetic phase diagram with different electronic densities and different electronic correlation strengths, using the Lanczos method we calculated the spin structure factor, which is defined as the Fourier transform of the spin-

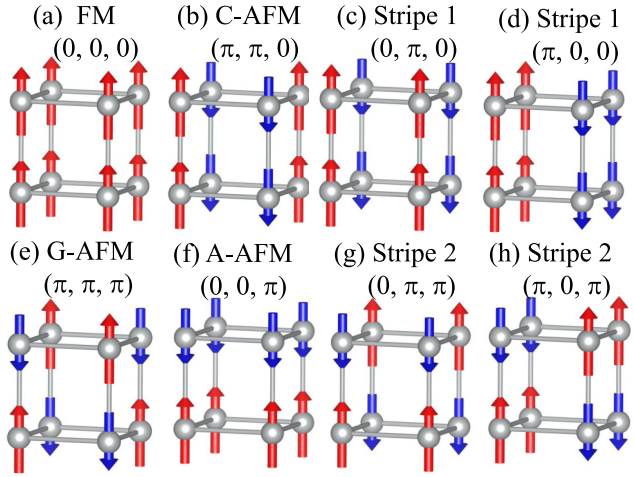

FIG. 2. Sketches of the observed magnetic structures for our $2 \times 2 \times 2$ system, including (a) FM, (b) C-AFM, (c) Stripe 1, (d) Stripe 1, (e) G-AFM, (f) A-AFM, (g) Stripe 2, and (h) Stripe 2, with the $S(\boldsymbol{q})$ peaks at $\boldsymbol{q}$ = (a) (0, 0, 0), (b) $(\pi, \pi, 0)$, (c) $(0, \pi, 0)$, (d) $(\pi, 0, 0)$, (e) (π, π, π), (f) $(0, 0, \pi)$, (g) $(0, \pi, \pi)$, and (h) $(\pi, 0, \pi)$, respectively. The arrows refer to spin up or spin down on each site of Ni. For the readers benefit, the spin up and spin down are also distinguished by different colors.

spin correlation function,

$$S(\boldsymbol{q}) = \frac{1}{N} \sum_{i,j} \langle \boldsymbol{S}_i \cdot \boldsymbol{S}_j \rangle e^{i\boldsymbol{q}\cdot(\boldsymbol{r}_i - \boldsymbol{r}_j)}, \tag{6}$$

where $\boldsymbol{S}_i$ is the spin at site i, $\boldsymbol{r}_i$ is the position of site i, $\langle \boldsymbol{S}_i \cdot \boldsymbol{S}_j \rangle$ is the average of real-space spin-spin correlation between sites i and j, N is the total number of lattice sites, and $\boldsymbol{q}$ is the wave vector.

We show all the magnetic structures observed for a $2 \times 2 \times 2$ system in Fig. 2, which includes FM, C-AFM, Stripe 1 (two energy degenerate variations), G-AFM, A-AFM, Stripe 2 (two energy degenerate variations), corresponding to the $S(\boldsymbol{q})$ peak at $\boldsymbol{q}$= (0, 0, 0), $(\pi, \pi, 0)$, $(0, \pi, 0)$, $(\pi, 0, 0)$, (π, π, π), $(0, 0, \pi)$, $(0, \pi, \pi)$, and $(\pi, 0, \pi)$, respectively. Because of rotational symmetry, $S(0, \pi, \pi)$ [$S(0, \pi, 0)$] and $S(\pi, 0, \pi)$ [$S(\pi, 0, 0)$] should be the same, which represents the Stripe 2 [1] phase.

Based on the measurements of the spin structure factor $S(\boldsymbol{q})$, we obtained the magnetic phase diagram for different electron numbers N and electronic correlations U/W, at fixed $J_H/U = 0.2$ as in our previous studies [48]. Results are shown in Fig. 3. Here, we considered the cases PBC and OBC. The results are similar for the two boundary conditions. Several interesting magnetic states emerge in the phase diagrams. At the half-filling situation ($N = 16$), the G-AFM is dominant in a robust manner for all values of U/W studied. By hole or electron doping away from the half-filling $N = 16$ case, the magnetic phases display a rich behavior because of the multiorbital nature of the model. The states reached by doping involve paramagnetism (PM), A-AFM, Stripe 2, C-AFM, and Stripe 1. In addition, the spin-spin correlations also become weaker in the hole or electronic doping regions, compared to the half-filling $N = 16$ case. Note that there is a slight difference between the cases of PBC and OBC. This is because in PBC, the t_x/t_y needs to be considered doubled in strength, as already explained, but only once in OBC, leading to a stronger AFM vs. FM competition in the xy plane in the PBC case.

For the benefit of the readers, in Fig. 4 we also show the detailed spin structure factors $S(\boldsymbol{q})$ for different spin states vs N, all at $U/W = 3$. For $N \lesssim 8$ and $\gtrsim 24$, the $S(\boldsymbol{q})$ is quite weak without substantial differences in peak strengths among different spin states, overall indicating PM. For other electronic densities, such $N = 10, 12, 16$, and 18, the peaks of $S(\boldsymbol{q})$ are located at $\boldsymbol{q} = (0, 0, \pi)$, $(0, \pi, \pi)/(\pi, 0, \pi)$, (π, π, π), and $(\pi, \pi, 0)$, corresponding to the A-AFM, Stripe 2, G-AFM, and C-AFM phases, respectively. By reproducing the same analysis of $U/W = 3$ for other values of U/W, we obtained the phase diagrams in Fig. 3.

C. Intuitive explanation of the phase diagram

Let us discuss now the intuitive explanation for the existence of the main phases at several key number of electrons

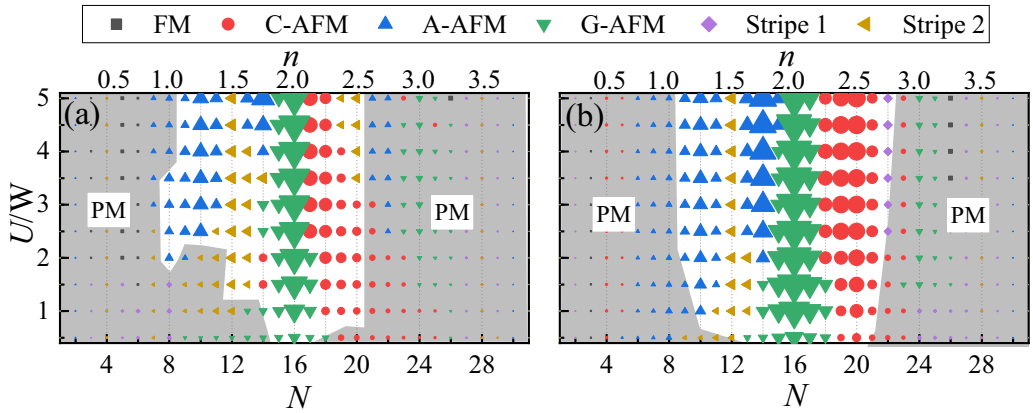

FIG. 3. Magnetic phase diagram of the small cluster studied here, varying U/W and N (n), at fixed $J_H/U = 0.2$. N means the total number of electrons for the $2 \times 2 \times 2$ model while n means the average number of electrons per site. Different magnetic phases, including FM, C-AFM, A-AFM, G-AFM, Stripe 1, and Stripe 2, are indicated by different points with different shapes and colors. The size of the points is proportional to the strength of the spin structure factor $S(\boldsymbol{q})$. For simplicity, the regions with $S(\boldsymbol{q}) \lesssim 2$ are marked as PM by using a gray color [using the number 2 as cutoff appears arbitrary, but for comparison the largest $S(\boldsymbol{q})$ is $\approx$10 at $U/W = 5$, $N = 16$, and OBC]. (a) is using PBC while (b) is using OBC.

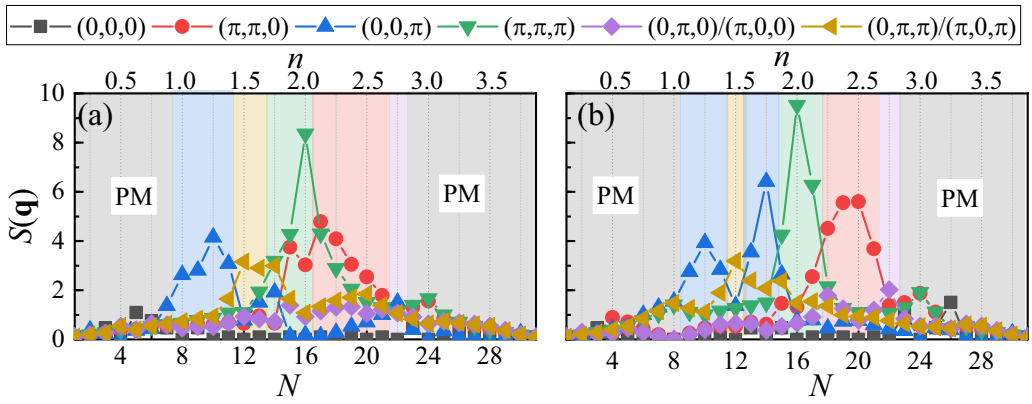

FIG. 4. The dominant spin structure factors for different spin states, as a function of different values of N (n) at $U/W = 3$ for the cases of (a) PBC and (b) OBC.

$N = 10$, 12, 16, and 18. This can be understood by three main coupling mechanisms [77,82,83], based on two-site second-order perturbation theory: (1) half-empty FM coupling, (2) half-half AFM coupling, and (3) half-full FM coupling. More specifically, (1) suppose there is overlap between a half-filled orbital (O1) and an empty orbital (O2), where O2 is Hund coupled with other partially occupied orbitals (O3). Then, the electron transfer between these half-filled and empty orbitals prefers to be parallel to the spin of O3, resulting in a FM coupling. (2) If there is overlap between two half-filled orbitals, then the electrons transfer between these orbitals must be antiparallel because of the Pauli exclusion principle, resulting in an AFM coupling. (3) If there is overlap between the half-filled orbital (O1) and full orbital (O2), and O2 is Hund coupled with other partially occupied orbitals (O3), then the only electron transfer possible is from O2 to O1 and back. The spin of the transfer electron in O2 must be antiparallel to the spin in O3 and O1, resulting in atomically FM coupling between O1 and O2+O3. Here, we also display the sketches of intuitive explanations of these main phases in Fig. 5. First, let us focus on the z direction, for $N = 10$, 12, and 16. Only the "half-half" AFM coupling mechanism (standard superexchange) is responsible for those cases as displayed in Figs. 5(a)–5(c), thus the AFM coupling is obtained, corresponding to the $S(\boldsymbol{q})$ peak at π along the z direction.

By increasing N, because of more than two electrons per two orbitals per site, the "half-full" FM coupling mechanism starts influencing on the energy of the many phases. This introduces competition between FM and AFM bonds at various values of N, leading to the C-AFM phase at $N = 18$ (see, as example, the detailed second-order perturbation theory analysis in Appendix A).

Now let us analyze the situation for the xy plane. For the half-filling $N = 16$ case, the canonical superexchange half-half AFM coupling leads to a robust G-AFM order. Correspondingly, the $S(\boldsymbol{q})$ peak is at (π, π) along the xy direction. (1) In the hole doping region away from half-filling, the AFM coupling caused by superexchange strongly competes with the FM coupling caused by the "half-empty" mechanism [77], leading to an in-plane stripe phase (AFM in one direction and FM in the other), such as Stripe 2 at $N = 12$. At $N = 10$, the FM tendency wins over AFM tendency in-plane, leading to in-plane FM coupling (AFM along z axis as analyzed in the previous paragraph), resulting in a global A-FM phase. (2) In the electron doping region away from half-filling, because of the "half-half" mechanism [84] AFM coupling wins, resulting at $N = 18$ in a C-AFM state (AFM coupling along the xy plane and FM coupling along the z axis). Increasing N further, the FM coupling caused by "half-full" mechanism starts playing an important role, competing with AFM coupling from "half-half" mechanism, resulting in the Stripe 1 phase (AFM in-plane in one direction and FM in the other, while it is FM along the z axis) for OBC, and A-AFM and C-AFM phases for PBC at $N = 22$ [see Figs. 3(a) and 3(b)].

For the $N = 12$ case—with average electronic density $n = 1.5$ per site corresponding to $La_3Ni_2O_7$ in our $2 \times 2 \times 2$ cluster calculations—we obtained a Stripe 2 phase [with wavevectors $(\pi, 0, \pi)$ or $(0, \pi, \pi)$], in agreement with previous theoretical studies using RPA [50,55]. This is quite remarkable, namely studying a small system and solving it exactly, gives very similar conclusions as RPA for the realistic electronic density $n = 1.5$, with RPA study done by us and

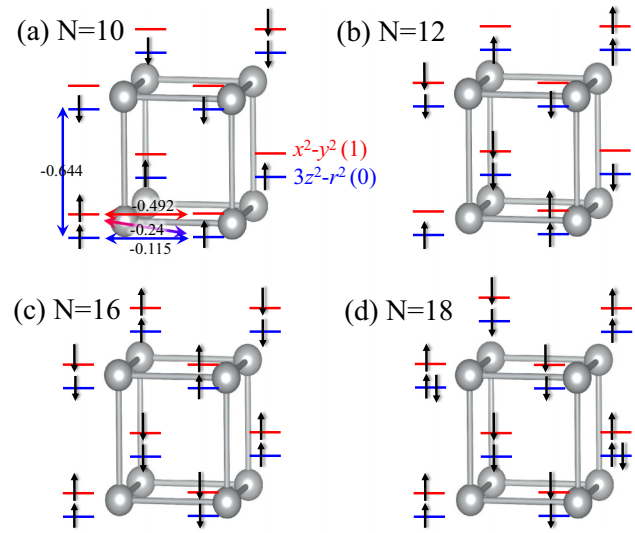

FIG. 5. Electronic configurations for some typical values of N, including (a) 10, (b) 12, (c) 16, and (d) 18. Here, the spin up and down are marked by arrows and the different orbitals are distinguished by different colors.

other groups. Note that RPA is based on a totally different many-body technique, sum of an infinite subset of Feynman diagrams as compared to solving exactly a small cluster.

Furthermore, we found that the AFM spin-spin correlations along the z axis are much stronger than the spin-spin correlations along the xy plane, which is in good agreement with recent experiments [70,71]. For example, for the $N = 12$ case with $U/W = 3$, $J_H/U = 0.2$, $\langle \boldsymbol{S}_i \cdot \boldsymbol{S}_j \rangle = -0.897$ along z axis while it is -0.054 along x and y direction. The reasons are (1) the hoppings along z direction are larger than the ones in xy plane, (2) because of the degeneracy of the $(\pi, 0, \pi)$ and $(0, \pi, \pi)$ states, the xy plane nearest spin-spin correlations have up-down, down-up, up-up, and down-down cases, so they canceled out with each other.

It should be noticed that for the real samples of $La_3Ni_2O_7$, experiments found oxygen deficiencies [19], leading to "effectively" varying the electronic density in the Ni site, away from $n = 1.5$. Thus, the AFM coupling in between planes should be very robust against oxygen deficiency. But along the in-plane directions, we found a strong FM vs AFM competition even just slightly varying the number of electrons (such as Stripe 2 at $N = 12$ and A-AFM at $N = 13$), suggesting that the oxygen deficiency may seriously affect the magnetic coupling along the in-plane directions in real samples.

Note that for a larger size system, unreachable using Lanczos because of the exponential increase in the size of the Hilbert space, the magnetic phase diagram could be even richer owing to in-plane FM and AFM competition. Specifically, because of these size limitations in clusters that can be studied with Lanczos, we could not explore other complex magnetic states, such as the E-AFM [85], CE-AFM [86], and block states [87], as well as possible charge or spin density wave states. In fact, very recent DFT calculations suggested that the E-AFM ground state dominates at ambient pressure [88–90]. Such a more complex structure as the E-AFM phase cannot fit into our small cluster, thus we cannot confirm or deny the existence of this state and other. Alternative (all approximate) many-body techniques, like unrestricted Hartree-Fock [91–93] will be needed to address this issue. The E-phase notation, widely used in manganites, is often referred to as double-stripe in nickelates.

In summary, in spite of their limitations, our calculations clearly reveal (1) Stripe 2 dominance at $n = 1.5$ as found via other many-body techniques, (2) a much stronger AFM coupling along the z axis than along the xy plane, (3) strong AFM and FM competition in the xy plane when moving slightly away from $n = 1.5$, (4) reduced spin spin correlations as compared with half-filing $N = 16$, and (5) a rich phase diagram varying N that merits experimental confirmation via chemical doping.

D. RPA results

We have also used the RPA method to quantify the magnetic properties of this bilayer system, varying the electronic density n. Past analyses have shown that the RPA, which is based on a perturbative weak-coupling expansion in the Hubbard interaction [94–97], captures the essence of the physics for Fe-based and Cu-based superconductors. Reference [95] provides background information, and we expect the RPA then to succeed also for Ni-based superconductors.

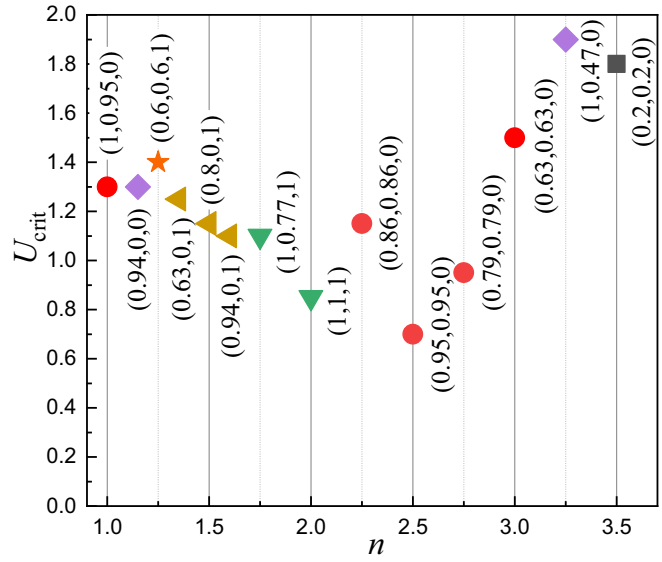

FIG. 6. RPA leading states with their vector q (in vertical parenthesis, in units of π) and U_{crit} vs n, where U_{crit} is the critical U for the magnetic instability within RPA.

Specifically, we analyze the RPA enhanced spin susceptibility tensor $\chi(\mathbf{q}, \omega = 0)$ that is obtained from the Lindhart function tensor $\chi_0(\mathbf{q})$ as

$$\chi(\mathbf{q}) = \chi_0(\mathbf{q})[1 - \mathcal{U}\chi_0(\mathbf{q})]^{-1}. \tag{7}$$

Here, $\chi_0(\mathbf{q})$ is an orbital-dependent susceptibility tensor and $\mathcal{U}$ is a tensor containing the interaction parameters [95].

Figure 6 shows U_{crit}, the critical value of U, for which the susceptibility $\chi(\mathbf{q})$ in Eq. (7) diverges, as a function of filling n, and the corresponding wavevector q of the instability. We note that, unlike in the Lanzcos, in the RPA this SDW instability generally occurs for incommensurate wavevector $\mathbf{q}$. At $n = 1.5$, the RPA found a state with $\mathbf{q} = (0.8, 0, 1)$ in units of π, thus resembling the Stripe 2 state of the Lanczos results with $\mathbf{q} = (1, 0, 1)$ in units of π. At larger n, the RPA finds states close to the G-AFM, C-AFM, and FM states as N increases, in close agreement with our Lanczos phase diagram. In the RPA, we do not find the A-AFM state for smaller n. However, as shown in Fig. 3(a), in the Lanzcos this state primarily occurs for $U/W \gtrsim 2$, i.e., much larger U than the U_{crit} of the RPA and beyond the range of U where the weak coupling RPA is applicable. In fact, for $U \lesssim U_{crit}$, where the RPA is expected to give accurate results, there is excellent agreement between both techniques. Furthermore, we also found a state with $\mathbf{q} = (0.6, 0.6, 1)$ close to the E-phase wavevector by slightly reducing the filling to $n = 1.25$, which is possibly responsible for the SDW discussed in recent experiments [70,75].

IV. DISCUSSION

This bilayer nickelate superconductor $La_3Ni_2O_7$ naturally reminds us of the previously well-studied infinite-layer nickelates and cuprates superconductors. As discussed in our previous paper [48], the $d_{3z^2-r^2}$ orbital displays a different behavior in bilayer $La_3Ni_2O_7$: showing bonding–antibonding states with a splitting induced by the canonical "dimer"

physics in the bilayer lattice. Furthermore, because of the absence of apical oxygen, a large in-plane *interorbital* hopping between $d_{3z^2-r^2}$ and $d_{x^2-y^2}$ orbitals was obtained in $La_3Ni_2O_7$, leading to a strong AFM and FM competition in the plane. However, this hopping is nearly zero in the infinite-layer nickelate, resulting in a strong AFM tendency in-plane. Recent experimental and theoretical studies suggest that infinite-layer nickelate superconductors can be described as a single $d_{x^2-y^2}$ Mott Hubbard system where in-plane AFM spin interactions drive the electron pairing [98,99].

In addition, the magnetic coupling between layers is weak in the infinite-layer nickelate but the magnetic coupling along the z axis is much stronger in $La_3Ni_2O_7$ caused by $d_{3z^2-r^2}$ orbitals. Thus, two orbitals are needed to capture the main physics of $La_3Ni_2O_7$. Although this bonding–antibonding splitting of the $d_{3z^2-r^2}$ orbital is also obtained in another bilayer $La_3Ni_2O_6$ [22], where the apical oxygen is missing as well, those states are far away from Fermi surface, suggesting a different role of the $d_{3z^2-r^2}$ orbital compared to $La_3Ni_2O_7$.

The nickelates show many similarities with cuprates, but also have fundamental differences, as discussed in the context of the infinite nickelate context [3,6,100]. Similar to other nickelates, the charge transfer gap between O's p and Ni's d orbitals in $La_3Ni_2O_7$ [48], shares the common nature of nickelates that they are closer to Mott Hubbard systems. But this charge-transfer gap is much smaller in the cuprate superconductors, resulting in a charge-transfer system [5]. Furthermore, it is widely believed that superconductivity is driven by the in-plane AFM fluctuations of the $d_{x^2-y^2}$ orbital in the cuprates, leading to d-wave superconductivity [9]. However, the strong interlayer coupling caused by the $d_{3z^2-r^2}$ orbital leads to possible $s_{\pm}$-wave pairing superconductivity in $La_3Ni_2O_7$ [43,50,54–61]. All these strongly indicate that the $La_3Ni_2O_7$ system is quite unique, different from both IL nickelates and cuprates superconductors, as well as from another bilayer $La_3Ni_2O_6$.

V. CONCLUSIONS

In summary, motivated by the recently discovered bilayer nickelate superconductor $La_3Ni_2O_7$, here we theoretically studied a bilayer $2 \times 2 \times 2$ cluster by using the Lanczos method, as well as the RPA in the weak-coupling region. A remarkably rich magnetic phase diagram was obtained, involving a variety of phases, such as the A-AFM, Stripe 2, Stripe 1, G-AFM, and C-AFM phases. Overall, this unusual variety is caused by the strong competition between FM and AFM tendencies at different electronic densities n per Ni. For $n = 1.5$, corresponding to $La_3Ni_2O_7$, in our $2 \times 2 \times 2$ cluster calculations we obtained the Stripe 2 ground state (AFM in one in-plane direction, FM in the other, while AFM along the z axis). Furthermore, we also obtained a much stronger AFM coupling along the z axis than the magnetic coupling in the xy plane. In addition, we observed a strong AFM vs FM competition in the xy plane. Note that if larger cluster sizes were available for Lanczos, other even more complex interesting phases could become stable, such as the E-AFM, CE-AFM, and block states, as extensively discussed in the case of manganites and iron-based superconductors [85–87]. Meanwhile, a state with $\mathbf{q} = (0.6, 0.6, 1)$ close to the E-phase wavevector is found in our RPA calculations by slightly reducing the filling to $n = 1.25$, which is possibly responsible to the SDW as discussed in the recent experiments. By hole or electronic doping away from half-filling $n = 2$, the spin-spin correlations become weaker as the doping increases in both directions. Thus, our results provide clear predictions of novel states for future experiments on Ni-oxide bilayer superconductors once the electronic density is varied via proper chemical doping.

Note added. Recently, we noticed that an independent theoretical study also showed similar results by using the RPA method varying the density n [101].

ACKNOWLEDGMENTS

We appreciate inspiring discussions with B. Pandey and P. Laurell. This work was supported by the U.S. Department of Energy, Office of Science, Basic Energy Sciences, Materials Sciences and Engineering Division. G.A. was supported by the U.S. Department of Energy, Office of Science, National Quantum Information Science Research Centers, and Quantum Science Center. G.A. contributed his expertise with the DMRG algorithm, its applicability to the multiorbital $2 \times 2 \times 2$ cube, and the software implementation.

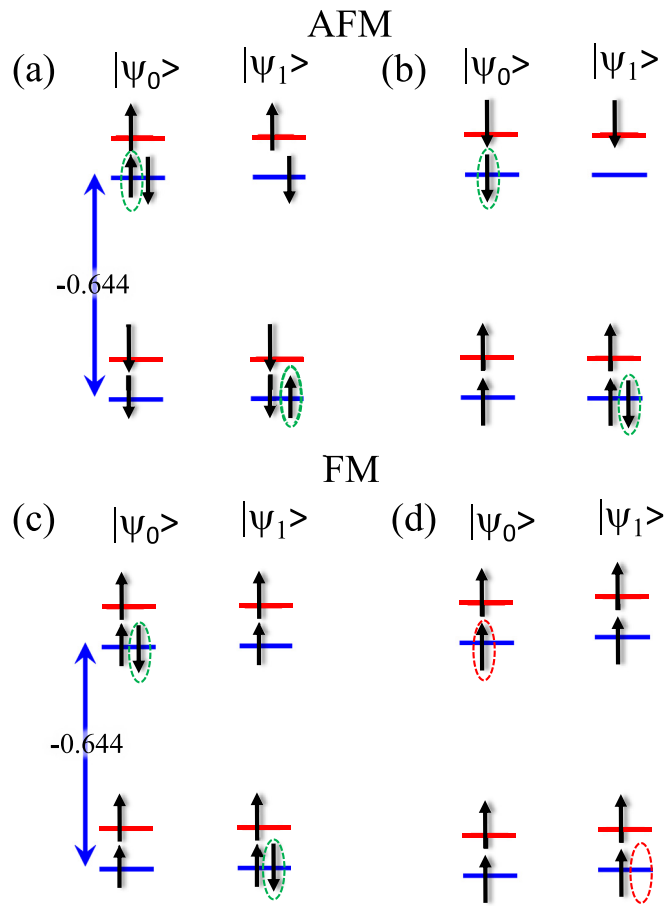

FIG. 7. Sketches of the virtual hopping process for $N = 18$ along the z direction. For simplicity, 2 sites with 2 orbitals are considered for both the AFM and FM cases. (a) and (c) are for 5 electrons, while (b) and (d) are for 4 electrons. Note that for the case (d), the hopping is forbidden (red dash ovals) because of the Pauli exclusion principle.

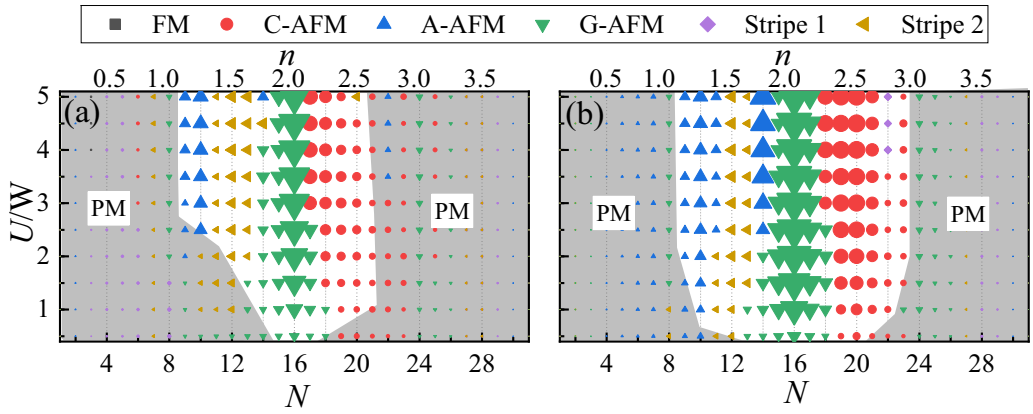

FIG. 8. Magnetic phase diagram of the $2 \times 2 \times 2$ cluster by varying U/W and N, at fixed $J_\mathrm{H}/U = 0.1$. Different magnetic phases, including FM, C-AFM, A-AFM, G-AFM, Stripe 1, and Stripe 2, are indicated by different points with different shapes and colors. The size of the points is proportional to the strength of the spin structure factor $S(\boldsymbol{q})$. For simplicity, the regions with $S(\boldsymbol{q}) \lesssim 2$ are marked as PM by using a gray color. (a) is using PBC while (b) is using OBC.

APPENDIX A: SECOND-ORDER PERTURBATION THEORY ANALYSIS FOR $N = 18$

For the benefit of the readers, we include here our study for $N = 18$, with focus on the z direction, to show the detailed two-site second-order perturbation theory analysis in the atomic limit, as illustrated in Fig. 7. Here the hopping $t_{00}^z = -0.644$ eV is treated as perturbation in the large U/W limit and we focus on the effect of the U, U', and Hund's coupling terms. For nondegenerate states [cases (a) and (b)], it is well known that second-order perturbation theory always lowers the energy by

$$\Delta E = -\sum_m \frac{|\langle\psi_m|H'|\psi_0\rangle|^2}{E_m - E_0}. \tag{A1}$$

For case (a), the ground state and first excited state atomic energies, starting point of the perturbation theory, are

$$E_0 = U + 3U' - J_\mathrm{H}, \tag{A2}$$

$$E_1 = U + 3U' + J_\mathrm{H}, \tag{A3}$$

respectively.

By using second-order perturbation theory, it can be shown that the energy gain of the AFM configuration [case (a)] owing to t_{00}^z is

$$\Delta E_{(\mathrm{a})} = \frac{|\langle\psi_1|H'|\psi_0\rangle|^2}{E_0 - E_1} = -\frac{|t_{00}^z|^2}{2J_\mathrm{H}}. \tag{A4}$$

Repeating the calculation for case (b), the ground state and excited state atomic energies are

$$E_0 = 2U' - 2J_\mathrm{H}, \tag{A5}$$

$$E_1 = U + 2U', \tag{A6}$$

respectively.

Then, the energy gain of the AFM configuration for case (b) is

$$\Delta E_{(\mathrm{b})} = \frac{|\langle\psi_1|H'|\psi_0\rangle|^2}{E_0 - E_1} = -\frac{|t_{00}^z|^2}{U + 2J_\mathrm{H}}. \tag{A7}$$

For the FM case (c), the two energy eigenstates of the unperturbed Hamiltonian are degenerate

$$E_0 = E_1 = U + 3U' - J_\mathrm{H}. \tag{A8}$$

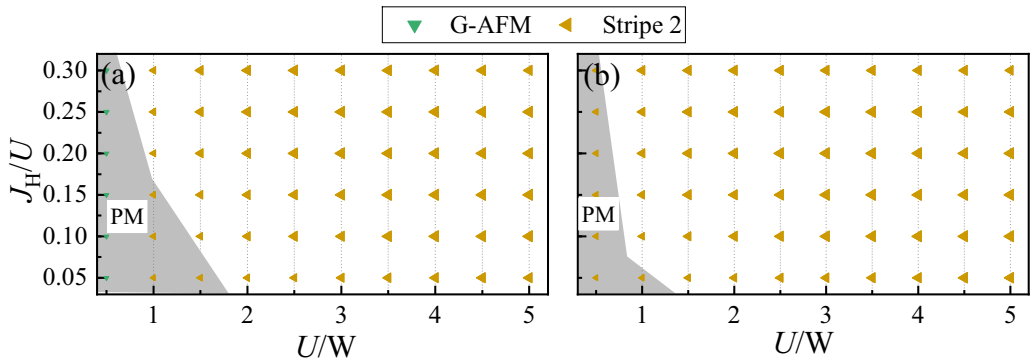

FIG. 9. Magnetic phase diagram of the $2 \times 2 \times 2$ cluster by varying U/W and J_H/U at fixed $N = 12$. Different magnetic phases, including G-AFM, and Stripe 2, are indicated by different points with different shapes and colors. The size of the points is proportional to the strength of the spin structure factor $S(\boldsymbol{q})$. For simplicity, the regions with $S(\boldsymbol{q}) \lesssim 2$ are marked as PM by using a gray color. (a) is using PBC while (b) is using OBC.

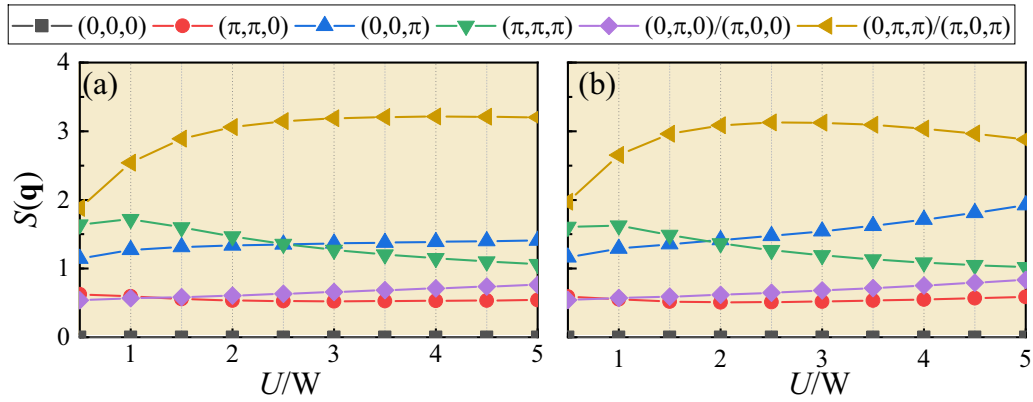

FIG. 10. Spin structure factor $S(\boldsymbol{q})$ of $2 \times 2 \times 2$ cluster as varying U/W at fixed $N = 12$ ($n = 1.5$). (a) Only nearest hoppings are included. (b) The next-nearest hoppings are also included. Here we only considered OBC.

Thus, we should mix those degenerate eigenstates to obtain the energy difference as

$$\begin{bmatrix} E_0 & t_{00}^z \\ t_{00}^z & E_0 \end{bmatrix} \begin{bmatrix} \psi_0 \\ \psi_1 \end{bmatrix} = E \begin{bmatrix} \psi_0 \\ \psi_1 \end{bmatrix}.$$

We obtain $E_\pm = E_0 \pm t_{00}^z$, so $\Delta E_{(c)} = t_{00}^z$.

For the FM case (d), hopping is forbidden because of the Pauli principle, so there is no energy gain.

By using $U/W = 3$ and the hoppings in the Methods section (Sec. II), at $J_\mathrm{H}/U = 0.2$, the total energy gained in the AFM state from t_{00}^z is ∼0.113 eV, which is smaller than the total energy gained from the FM state which is ∼0.644 eV. This result indicates the FM case wins over AFM. Thus, along the z axis a transition from wavevector π for hole doping to wavevector 0 for electron doping is expected, in excellent agreement with the Lanczos results.

APPENDIX B: LANCZOS PHASE DIAGRAMS AT $J_H/U = 0.1$

As shown in Fig. 8, we also calculated the Lanczos phase diagrams at $J_\mathrm{H}/U = 0.1$. Those results were found to be similar to the case $J_\mathrm{H}/U = 0.2$, indicating that our overall results are robust against changes in J_H/U.

APPENDIX C: LANCZOS PHASE DIAGRAMS AT $n = 1.5$

As shown in Fig. 9, we also calculated the Lanczos phase diagrams by varying U/W and J_H/U at fixed $N = 12$. The Stripe 2 state is robust against by changing in J_H/U and U/W.

APPENDIX D: EFFECT OF NEXT-NEAREST-NEIGHBORS HOPPINGS

The three next-nearest-hopping matrices (in eV units) are shown below:

$$t_{\gamma\gamma'}^{x+z} = \begin{bmatrix} 0.025 & -0.039 \\ -0.039 & 0 \end{bmatrix}, \tag{D1}$$

$$t_{\gamma\gamma'}^{y+z} = \begin{bmatrix} 0.025 & 0.039 \\ 0.039 & 0 \end{bmatrix}, \tag{D2}$$

$$t_{\gamma\gamma'}^{x+y} = \begin{bmatrix} -0.014 & 0.000 \\ 0.00 & 0.066 \end{bmatrix}. \tag{D3}$$

All the next-nearest-hopping matrix elements are much smaller than the nearest-neighbor-hopping matrix elements. As shown in Fig. 10, we also studied the spin structure factors for different spin states at $n = 1.5$ by involving next-nearest hoppings while varying U/W, finding that the stripe 2 order is still robust. We also recalculated RPA results after including next-nearest hoppings, as shown in Fig. 11. It is clear that stripe 2 order is still robust at $n = 1.5$. We also noticed that there are some small changes of the wavevector q and the critical U after introducing next-nearest-neighbors hoppings. This is reasonable because RPA calculations are very sensitive to small changes in the dispersion and Fermi surface.

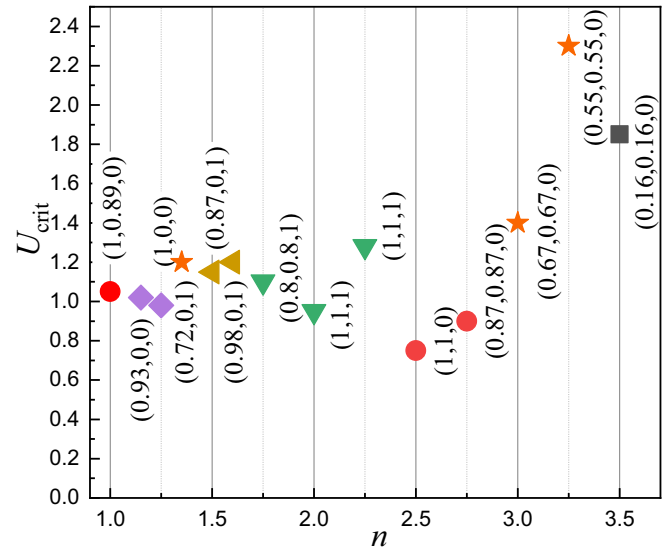

FIG. 11. RPA leading states with their vector q (in vertical parenthesis, in units of π) and U_crit vs n after including next-nearest hoppings, where U_crit is the critical U for the magnetic instability within RPA.

[1] D. Li, K. Lee, B. Y. Wang, M. Osada, S. Crossley, H. R. Lee, Y. Cui, Y. Hikita, and H. Y. Hwang, Superconductivity in an infinite-layer nickelate, Nature (London) **572**, 624 (2019).

[2] G. A. Pan, D. F. Segedin, H. LaBollita, Q. Song, E. M. Nica, B. H. Goodge, A. T. Pierce, S. Doyle, S. Novakov, D. C. Carrizales *et al.*, Superconductivity in a quintuple-layer square-planar nickelate, Nat. Mater. **21**, 160 (2022).

[3] A. S. Botana, and M. R. Norman, Similarities and differences between $LaNiO_2$ and $CaCuO_2$ and implications for superconductivity, Phys. Rev. X **10**, 011024 (2020).

[4] Y. Nomura, and R. Arita, Superconductivity in infinite-layer nickelates, Rep. Prog. Phys. **85**, 052501 (2022).

[5] Y. Zhang, L.-F. Lin, W. Hu, A. Moreo, S. Dong, and E. Dagotto, Similarities and differences between nickelate and cuprate films grown on a $SrTiO_3$ substrate, Phys. Rev. B **102**, 195117 (2020).

[6] K.-W. Lee and W. E. Pickett, Infinite-layer $LaNiO_2$: Ni^{1+} is not Cu^{2+}, Phys. Rev. B **70**, 165109 (2004).

[7] Q. Gu and H.-H. Wen, Superconductivity in nickel-based 112 systems, Innovation **3**, 100202 (2022).

[8] J. G. Bednorz and K. A. Müller, Possible high T_c superconductivity in the Ba-La-Cu-O system, Z. Phys. B: Condens. Matter **64**, 189 (1986).

[9] E. Dagotto, Correlated electrons in high-temperature superconductors, Rev. Mod. Phys. **66**, 763 (1994).

[10] Y. Kamihara, T. Watanabe, M. Hirano, and H. Hosono, Iron-based layered superconductor $La[O_{1-x}F_x]FeAs$ ($x = 0.05 - 0.12$) with $T_c = 26$ K, J. Am. Chem. Soc. **130**, 3296 (2008).

[11] E. Dagotto, *Colloquium*: The unexpected properties of alkali metal iron selenide superconductors, Rev. Mod. Phys. **85**, 849 (2013).

[12] H. Sun, M. Huo, X. Hu, J. Li, Y. Han, L. Tang, Z. Mao, P. Yang, B. Wang, J. Cheng *et al.*, Signatures of superconductivity near 80 K in a nickelate under high pressure, Nature (London) **621**, 493 (2023).

[13] Z. Liu, M. Huo, J. Li, Q. Li, Y. Liu, Y. Dai, X. Zhou, J. Hao, Y. Lu, M. Wang, and W.-H. Wen, Electronic correlations and partial gap in the bilayer nickelate $La_3Ni_2O_7$, Nat. Commun. **15**, 7570 (2024).

[14] Y. Zhang, D. Su, Y. Huang, H. Sun, M. Huo, Z. Shan, K. Ye, Z. Yang, R. Li, M. Smidman *et al.*, High-temperature superconductivity with zero-resistance and strange metal behavior in $La_3Ni_2O_{7-\delta}$, Nat. Phys. **20**, 1269 (2024).

[15] J. Hou, P. T. Yang, Z. Y. Liu, J. Y. Li, P. F. Shan, L. Ma, G. Wang, N. N. Wang, H. Z. Guo, J. P. Sun *et al.*, Emergence of high-temperature superconducting phase in pressurized $La_3Ni_2O_7$ crystals, Chin. Phys. Lett. **40**, 117302 (2023).

[16] J. Yang, H. Sun, X. Hu, Y. Xie, T. Miao, H. Luo, H. Chen, B. Liang, W. Zhu, G. Qu *et al.*, Orbital-dependent electron correlation in double-layer nickelate $La_3Ni_2O_7$, Nat. Commun. **15**, 4373 (2024).

[17] M. Zhang, C. Pei, Q. Wang, Y. Zhao, C. Li, W. Cao, S. Zhu, J. Wu, and Y. Qi, Effects of pressure and doping on Ruddlesden-Popper phases $La_{n+1}Ni_nO_{3n+1}$, J. Mater. Sci. Technol. **185**, 147 (2024).

[18] G. Wang, N. N. Wang, X. L. Shen, J. Hou, L. Ma, L. F. Shi, Z. A. Ren, Y. D. Gu, H. M. Ma, P. T. Yang, Z. Y. Liu, H. Z. Guo, J. P. Sun, G. M. Zhang, S. Calder, J.-Q. Yan, B. S. Wang, Y. Uwatoko, and J.-G. Cheng, Pressure-induced superconductivity in polycrystalline $La_3Ni_2O_{7-\delta}$, Phys. Rev. X **14**, 011040 (2024).

[19] Z. Dong, M. Huo, Jie Li, Jingyuan Li, P. Li, H. Sun, L. Gu, Y. Lu, M. Wang, Y. Wang, and Z. Chen, Visualization of oxygen vacancies and self-doped ligand holes in $La_3Ni_2O_{7-\delta}$, Nature (London) **630**, 847 (2024).

[20] Y. Zhang, L.-F. Lin, A. Moreo, T. A. Maier, and E. Dagotto, Prediction of $s^{\pm}$-wave superconductivity enhanced by electronic doping in trilayer nickelates $La_4Ni_3O_{10}$ under pressure, Phys. Rev. Lett. **133**, 136001 (2024).

[21] Y. Zhang, L.-F. Lin, A. Moreo, T. A. Maier, and E. Dagotto, Magnetic correlations and pairing tendencies of the hybrid stacking nickelate superlattice $La_7Ni_5O_{17}$ ($La_3Ni_2O_7/La_4Ni_3O_{10}$) under pressure, arXiv:2408.07690.

[22] Y. Zhang, L.-F. Lin, A. Moreo, T. A. Maier, and E. Dagotto, Electronic structure, magnetic correlations, and superconducting pairing in the reduced Ruddlesden-Popper bilayer $La_3Ni_2O_6$ under pressure: Different role of $d_{3z^2-r^2}$ orbital compared with $La_3Ni_2O_7$, Phys. Rev. B **109**, 045151 (2024).

[23] M. Wang, H.-H. Wen, T. Wu, D.-X. Yao, and T. Xiang, Normal and superconducting properties of $La_3Ni_2O_7$, Chinese Phys. Lett. **41**, 077402 (2024).

[24] Y. Li, X. Du, Y. Cao, C. Pei, M. Zhang, W. Zhao, K. Zhai, R. Xu, Z. Liu, Z. Li *et al.*, Electronic correlation and pseudogap-like behavior of high-temperature superconductor $La_3Ni_2O_7$, Chinese Phys. Lett. **41**, 087402 (2024).

[25] H. Oh and Y.-H. Zhang, Type-II $t-J$ model and shared superexchange coupling from Hund's rule in superconducting $La_3Ni_2O_7$, Phys. Rev. B **108**, 174511 (2023).

[26] J.-R. Xue and F. Wang, Magnetism and superconductivity in the $t-J$ model of $La_3Ni_2O_7$ under multiband Gutzwiller approximation, Chinese Phys. Lett. **41**, 057403 (2024).

[27] D. Takegami, K. Fujinuma, R. Nakamura, M. Yoshimura, K.-D. Tsuei, G. Wang, N. N. Wang, J.-G. Cheng, Y. Uwatoko, and T. Mizokawa, Absence of Ni^{2+}/Ni^{3+} charge disproportionation and possible roles of O $2p$ holes in $La_3Ni_2O_{7-\delta}$ revealed by hard x-ray photoemission spectroscopy, Phys. Rev. B **109**, 125119 (2024).

[28] R. Jiang, J. Hou, Z. Fan, Z.-J. Lang, and W. Ku, Pressure driven fractionalization of ionic spins results in cupratelike high-Tc superconductivity in $La_3Ni_2O_7$, Phys. Rev. Lett. **132**, 126503 (2024.

[29] H. Sakakibara, M. Ochi, H. Nagata, Y. Ueki, H. Sakurai, R. Matsumoto, K. Terashima, K. Hirose, H. Ohta, M. Kato, Y. Takano, and K. Kuroki, Theoretical analysis on the possibility of superconductivity in the trilayer Ruddlesden-Popper nickelate $La_4Ni_3O_{10}$ under pressure and its experimental examination: Comparison with $La_3Ni_2O_7$, Phys. Rev. B **109**, 144511 (2024).

[30] L. Craco and S. Leoni, Strange metal and coherence-incoherence crossover in pressurized $La_3Ni_2O_7$, Phys. Rev. B **109**, 165116 (2024).

[31] S. Bötzel, F. Lechermann, J. Gondolf, and I. M. Eremin, Theory of magnetic excitations in the multilayer nickelate superconductor $La_3Ni_2O_7$, Phys. Rev. B **109**, L180502 (2024).

[32] M. Kakoi, T. Kaneko, H. Sakakibara, M. Ochi, and K. Kuroki, Pair correlations of the hybridized orbitals in a ladder model for the bilayer nickelate $La_3Ni_2O_7$, Phys. Rev. B **109**, L201124 (2024).

[33] J. Chen, F. Yang, and W. Li, Orbital-selective superconductivity in the pressurized bilayer nickelate $La_3Ni_2O_7$:An infinite projected entangled-pair state study, Phys. Rev. B **110**, L041111 (2024).

[34] B. Geisler, L. Fanfarillo, J. J. Hamlin, G. R. Stewart, R. G. Hennig, and P. J. Hirschfeld, Optical properties and electronic correlations in $La_3Ni_2O_{7-\delta}$ bilayer nickelates under high pressure, arXiv:2401.04258.

[35] H. Schlömer, U. Schollwöck, F. Grusdt, and A. Bohrdt, Superconductivity in the pressurized nickelate $La_3Ni_2O_7$ in the vicinity of a BEC-BCS crossover, arXiv:2311.03349.

[36] H. Yang, H. Oh, and Y.-H. Zhang, Strong pairing from small Fermi surface beyond weak coupling: Application to $La_3Ni_2O_7$, arXiv:2309.15095.

[37] H. Lange, L. Homeier, E. Demler, U. Schollwöck, F. Grusdt, and A. Bohrdt, Feshbach resonance in a strongly repulsive bilayer model: A possible scenario for bilayer nickelate superconductors, Phys. Rev. B **109**, 045127 (2024).

[38] T. Kaneko, H. Sakakibara, M. Ochi, and K. Kuroki, Pair correlations in the two-orbital Hubbard ladder: Implications for superconductivity in the bilayer nickelate $La_3Ni_2O_7$, Phys. Rev. B **109**, 045154 (2024).

[39] J. Huang, Z. D. Wang, and T. Zhou, Impurity and vortex states in the bilayer high-temperature superconductor $La_3Ni_2O_7$, Phys. Rev. B **108**, 174501 (2023).

[40] C. D. Ling, D. N. Argyriou, G. Wu, and J. J. Neumeier, Neutron diffraction study of $La_3Ni_2O_7$: Structural relationships among $n = 1$, 2, and 3 phases $La_{n+1}Ni_nO_{3n+1}$, J. Solid State Chem. **152**, 517 (2000).

[41] B. Geisler, J. J. Hamlin, G. R. Stewart, R. G. Hennig, and P. J. Hirschfeld, Structural transitions, octahedral rotations, and electronic properties of $A_3Ni_2O_7$ rare-earth nickelates under high pressure, npj Quantum Mater. **9**, 38 (2024).

[42] L. Wang, L. Wang, Y. Li, S.-Y. Xie, F. Liu, H. Sun, C. Huang, Y. Gao, T. Nakagawa, B. Fu *et al.*, Structure responsible for the superconducting state in $La_3Ni_2O_7$ at high-pressure and low-temperature conditions, J. Am. Chem. Soc. **146**, 7506 (2024).

[43] H. Sakakibara, N. Kitamine, M. Ochi, and K. Kuroki, Possible high T_c superconductivity in $La_3Ni_2O_7$ under high pressure through manifestation of a nearly half-filled bilayer Hubbard model, Phys. Rev. Lett. **132**, 106002 (2024).

[44] Y. Zhang, L.-F. Lin, A. Moreo, T. A. Maier, and E. Dagotto, Electronic structure, self-doping, and superconducting instability in the alternating single-layer trilayer stacking nickelates $La_3Ni_2O_7$, Phys. Rev. B **110**, L060510 (2024).

[45] J. Li, P. Ma, H. Zhang, X. Huang, C. Huang, M. Huo, D. Hu, Z. Dong, C. He, J. Liao, X. Chen, T. Xie, H. Sun, and M. Wang, Pressure-driven right-triangle shape superconductivity in bilayer nickelate $La_3Ni_2O_7$, arXiv:2404.11369.

[46] Y. Zhou, J. Guo, S. Cai, H. Sun, P. Wang, J. Zhao, J. Han, X. Chen, Y. Chen, Q. Wu, Y. Ding, T. Xiang, Ho-kwang Mao, and Liling Sun, Investigations of key issues on the reproducibility of high-*T*c superconductivity emerging from compressed $La_3Ni_2O_7$, arXiv:2311.12361.

[47] Z. Luo, X. Hu, M. Wang, W. Wu, and D.-X. Yao, Bilayer two-orbital model of $La_3Ni_2O_7$ under pressure, Phys. Rev. Lett. **131**, 126001 (2023).

[48] Y. Zhang, L.-F. Lin, A. Moreo, and E. Dagotto, Electronic structure, dimer physics, orbital-selective behavior, and magnetic tendencies in the bilayer nickelate superconductor $La_3Ni_2O_7$ under pressure, Phys. Rev. B **108**, L180510 (2023).

[49] V. Christiansson, F. Petocchi and P. Werner, Correlated electronic structure of $La_3Ni_2O_7$ under pressure, Phys. Rev. Lett. **131**, 206501 (2023).

[50] Y. Zhang, L.-F. Lin, A. Moreo, T. A. Maier, and E. Dagotto, Structural phase transition, $s_\pm$-wave pairing, and magnetic stripe order in bilayered superconductor $La_3Ni_2O_7$ under pressure, Nat. Commun. **15**, 2470 (2024).

[51] X.-W. Yi, Y. Meng, J.-W. Li, Z.-W. Liao, J.-Y. You, B. Gu, and G. Su, Nature of charge density waves and metal-insulator transition in pressurized $La_3Ni_2O_7$, Phys. Rev. B **110**, L140508 (2024).

[52] Z. Ouyang, M. Gao, and Z.-Y. Lu, Absence of electron-phonon coupling superconductivity in the bilayer phase of $La_3Ni_2O_7$ under pressure, npj Quantum Mater. **9**, 80 (2024).

[53] J. Zhang, Y. Gu, X. Wu, and J. Hu, Cooperation between electron-phonon coupling and electronic interaction in bilayer nickelates $La_3Ni_2O_7$, arXiv:2404.03638.

[54] Z. Liao, L. Chen, G. Duan, Y. Wang, C. Liu, R. Yu, and Q. Si, Electron correlations and superconductivity in $La_3Ni_2O_7$ under pressure tuning, Phys. Rev. B **108**, 214522 (2023).

[55] Y. Zhang, L.-F. Lin, A. Moreo, T. A. Maier, and E. Dagotto, Trends in electronic structures and $s_\pm$-wave pairing for the rare-earth series in bilayer nickelate superconductor $R_3Ni_2O_7$, Phys. Rev. B **108**, 165141 (2023).

[56] Q.-G. Yang, D. Wang, and Q.-H. Wang, Possible $s_\pm$-wave superconductivity in $La_3Ni_2O_7$, Phys. Rev. B **108**, L140505 (2023).

[57] Y. Gu, C. Le, Z. Yang, X. Wu, and J. Hu, Effective model and pairing tendency in bilayer Ni-based superconductor $La_3Ni_2O_7$, arXiv:2306.07275.

[58] Y. Shen, M. Qin, and G.-M. Zhang, Effective bi-layer model Hamiltonian and density-matrix renormalization group study for the high-T_c superconductivity in $La_3Ni_2O_7$ under high pressure, Chinese Phys. Lett. **40**, 127401 (2023).

[59] Y.-B. Liu, J.-W. Mei, F. Ye, W.-Q. Chen, and F. Yang, $s^\pm$-Wave pairing and the destructive role of apical-oxygen deficiencies in $La_3Ni_2O_7$ under pressure, Phys. Rev. Lett. **131**, 236002 (2023).

[60] X.-Z. Qu, D.-W. Qu, J. Chen, C. Wu, F. Yang, W. Li, and G. Su, Bilayer $t - J - J_\perp$ Model and magnetically mediated pairing in the pressurized nickelate $La_3Ni_2O_7$, Phys. Rev. Lett. **132**, 036502 (2024).

[61] C. Lu, Z. Pan, F. Yang, and C. Wu, Interlayer-coupling-driven high-temperature superconductivity in $La_3Ni_2O_7$ under pressure, Phys. Rev. Lett. **132**, 146002 (2024).

[62] Y.-H. Tian, Y. Chen, J.-M. Wang, R.-Q. He, and Z.-Y. Lu, Correlation effects and concomitant two-orbital $s_\pm$-wave superconductivity in $La_3Ni_2O_7$ under high pressure, Phys. Rev. B **109**, 165154 (2024).

[63] F. Lechermann, J. Gondolf, S. Bötzel, and I. M. Eremin, Electronic correlations and superconducting instability in $La_3Ni_2O_7$ under high pressure, Phys. Rev. B **108**, L201121 (2023).

[64] K. Jiang, Z. Wang, and F. Zhang, High-temperature superconductivity in $La_3Ni_2O_7$, Chin. Phys. Lett. **41**, 017402 (2024).

[65] Z. Fan, J.-F. Zhang, B. Zhan, D. Lv, X.-Y. Jiang, B. Normand, and T. Xiang, Superconductivity in nickelate and cuprate su-

perconductors with strong bilayer coupling, Phys. Rev. B **110**, 024514 (2024).
[66] H. Liu, C. Xia, S. Zhou, and H. Chen, Role of crystal-field-splitting and long-range-hoppings on superconducting pairing symmetry of $La_3Ni_2O_7$, arXiv:2311.07316.
[67] G. Heier, K. Park, and S. Y. Savrasov, Competing d_{xy} and $s_{\pm}$ pairing symmetries in superconducting $La_3Ni_2O_7$: LDA+FLEX calculations, Phys. Rev. B **109**, 104508 (2024).
[68] E. Dagotto, J. Riera, and D. Scalapino, Superconductivity in ladders and coupled planes, Phys. Rev. B **45**, 5744(R) (1992).
[69] G. Wu, J. J. Neumeier, and M. F. Hundley, Magnetic susceptibility, heat capacity, and pressure dependence of the electrical resistivity of $La_3Ni_2O_7$ and $La_4Ni_3O_{10}$, Phys. Rev. B **63**, 245120 (2001).
[70] X. Chen, J. Choi, Z. Jiang, J. Mei, K. Jiang, J. Li, S. Agrestini, M. Garcia-Fernandez, X. Huang, H. Sun, D. Shen, M. Wang, J. Hu, Y. Lu, K.-J. Zhou, and D. Feng, Electronic and magnetic excitations in $La_3Ni_2O_7$, Nat. Commun. **15**, 9597 (2024).
[71] T. Xie, M. Huo, X. Ni, F. Shen, X. Huang, H. Sun, H. C. Walker, D. Adroja, D. Yu, B. Shen, L. He, K. Cao, and M. Wang, Strong interlayer magnetic exchange coupling in $La_3Ni_2O_{7-\delta}$ revealed by inelastic neutron scattering, Sci. Bull. **69**, 3221 (2024).
[72] R. Khasanov, T. J. Hicken, D. J. Gawryluk, L. P. Sorel, S. Botzel, F. Lechermann, I. M. Eremin, H. Luetkens, and Z. Guguchia, Pressure-induced split of the density wave transitions in $La_3Ni_2O_{7-\delta}$, arXiv:2402.10485.
[73] Z. Liu, H. Sun, M. Huo, X. Ma, Y. Ji, E. Yi, L. Li, H. Liu, J. Yu, Z. Zhang *et al.*, Evidence for charge and spin density waves in single crystals of $La_3Ni_2O_7$ and $La_3Ni_2O_6$, Sci. China Phys. Mech. Astron. **66**, 217411 (2023).
[74] K. Chen, X. Liu, J. Jiao, M. Zou, C. Jiang, X. Li, Y. Luo, Q. Wu, N. Zhang, Y. Guo, and L. Shu, Evidence of spin density waves in $La_3Ni_2O_{7-\delta}$, Phys. Rev. Lett. **132**, 256503 (2024).
[75] Z. Dan, Y. Zhou, M. Huo, Y. Wang, L. Nie, M. Wang, T. Wu, and X. Chen, Spin-density-wave transition in double-layer nickelate $La_3Ni_2O_7$, arXiv:2402.03952.
[76] We have verified that exact diagonalization of the half-filled one orbital Hubbard model in a 2×2 cluster correctly indicates the (π, π) AFM order obtained in larger clusters.
[77] L. F. Lin, Y. Zhang, G. Alvarez, A. Moreo, and E. Dagotto, Origin of insulating ferromagnetism in iron oxychalcogenide $Ce_2O_2FeSe_2$, Phys. Rev. Lett. **127**, 077204 (2021).
[78] S. R. White, Density matrix formulation for quantum renormalization groups, Phys. Rev. Lett. **69**, 2863 (1992).
[79] S. R. White, Density-matrix algorithms for quantum renormalization groups, Phys. Rev. B **48**, 10345 (1993).
[80] https://github.com/nkphys/SCS_Lanczos.
[81] G. Alvarez, The density matrix renormalization group for strongly correlated electron systems: A generic implementation, Comput. Phys. Commun. **180**, 1572 (2009).
[82] L. F. Lin, Y. Zhang, G. Alvarez, M. A. McGuire, A. F. May, A. Moreo, and E. Dagotto, Stability of the interorbital-hopping mechanism for ferromagnetism in multi-orbital Hubbard models, Commun. Phys. **6**, 199 (2023).
[83] L. F. Lin, Y. Zhang, G. Alvarez, A. Moreo, Jacek Herbrych, and E. Dagotto, Prediction of orbital-selective Mott phases and block magnetic states in the quasi-one-dimensional iron chain $Ce_2O_2FeSe_2$ under hole and electron doping, Phys. Rev. B **105**, 075119 (2022).
[84] P. W. Anderson, Antiferromagnetism. Theory of superexchange interaction, Phys. Rev. **79**, 350 (1950).
[85] I. A. Sergienko, C. Şen, and E. Dagotto, Ferroelectricity in the magnetic e-phase of orthorhombic perovskites, Phys. Rev. Lett. **97**, 227204 (2006).
[86] S. Yunoki, T. Hotta, and E. Dagotto, Ferromagnetic, A-type, and charge-ordered CE-type states in doped manganites using Jahn-Teller phonons, Phys. Rev. Lett. **84**, 3714 (2000).
[87] Y. Zhang, L. Lin, J. Zhang, E. Dagotto, and S. Dong, Sequential structural and antiferromagnetic transitions in $BaFe_2Se_3$ under pressure, Phys. Rev. B **97**, 045119 (2018).
[88] H. LaBollita, V. Pardo, M. R. Norman, and A. S. Botana, Assessing the formation of spin and charge stripes in $La_3Ni_2O_7$ from first-principles, arXiv:2407.14409.
[89] B. Zhang, C. Xu, and H. Xiang, Emergent spin-charge-orbital order in superconductor $La_3Ni_2O_7$, arXiv:2407.18473.
[90] X.-S. Ni, Y. Ji, L. He, T. Xie, D.-X. Yao, M. Wang, and K. Cao, First-principles study on spin density wave in $La_3Ni_2O_{7-\delta}$, arXiv:2407.19213.
[91] L. Lin, N. Kaushal, Y. Zhang, A. Moreo, and E. Dagotto, Orbital ordering in the layered perovskite material $CsVF_4$, Phys. Rev. Mater. **5**, 025001 (2021).
[92] M. Daghofer, A. Nicholson, A. Moreo, and E. Dagotto, Three orbital model for the iron-based superconductors, Phys. Rev. B **81**, 014511 (2010).
[93] B. Pandey, Y. Zhang, N. Kaushal, R. Soni, L. Lin, W. Hu, G. Alvarez, and E. Dagotto, Origin of the magnetic and orbital ordering in α-Sr_2CrO_4, Phys. Rev. B **103**, 045115 (2021).
[94] K. Kubo, Pairing symmetry in a two-orbital Hubbard model on a square lattice, Phys. Rev. B **75**, 224509 (2007).
[95] S. Graser, T. A. Maier, P. J. Hirschfeld, and D. J. Scalapino, Near-degeneracy of several pairing channels in multiorbital models for the Fe pnictides, New J. Phys. **11**, 025016 (2009).
[96] M. Altmeyer, D. Guterding, P. J. Hirschfeld, T. A. Maier, R. Valentí, and D. J. Scalapino, Role of vertex corrections in the matrix formulation of the random phase approximation for the multiorbital Hubbard model, Phys. Rev. B **94**, 214515 (2016).
[97] A. T. Rømer, T. A. Maier, A. Kreisel, I. Eremin, P. J. Hirschfeld, and B. M. Andersen, Pairing in the two-dimensional Hubbard model from weak to strong coupling, Phys. Rev. Res. **2**, 013108 (2020).
[98] P. Worm, Q. Wang, M. Kitatani, I. Biało, Q. Gao, X. Ren, J. Choi, D. Csontosová, K.-J. Zhou, X. Zhou, Z. Zhu, L. Si, J. Chang, J. M. Tomczak, and K. Held, Spin fluctuations sufficient to mediate superconductivity in nickelates, Phys. Rev. B **109**, 235126 (2024).
[99] S. Zeng, C. S. Tang, Z. Luo, L. E. Chow, Z. S. Lim, S. Prakash, P. Yang, C. Diao, X. Yu, Z. Xing, R. Ji, X. Yin, C. Li, X. R. Wang, Q. He, M. B. H. Breese, A. Ariando, and H. Liu, Origin of a topotactic reduction effect for superconductivity in infinite-layer nickelate, Phys. Rev. Lett. **133**, 066503 (2024).
[100] J. Karp, A. S. Botana, M. R. Norman, H. Park, M. Zingl, and A. Millis, Many-body electronic structure of $NdNiO_2$ and $CaCuO_2$, Phys. Rev. X **10**, 021061 (2020).
[101] H. Zhang, Y. Bai, F. Kong, X. Wu, Y. Xing, and N. Xu, Doping evolution of the normal state magnetic excitations in pressurized $La_3Ni_2O_7$, arXiv:2408.03763.